

Quantization-Aware Neuromorphic Architecture for Efficient Skin Disease Classification on Resource-Constrained Devices

Haitian Wang[✉], Xinyu Wang[✉], Yiren Wang[✉], Zichen Geng[✉], Xian Zhang[✉], Yu Zhang[✉], Bo Miao[✉]

Abstract—On-device skin lesion edge classification remains hindered by the lack of efficient architectures compatible with neuromorphic deployment, as conventional CNN-to-SNN conversion suffers from structural incompatibility, performance degradation on rare diseases, and absence of continual learning. To address these limitations, we propose an end-to-end pipeline that incorporates a quantization-aware CNN backbone explicitly designed for conversion-preserving mapping to SNNs and neuromorphic deployment, culminating in the QANA architecture optimized for low-latency, energy-efficient, and incremental inference. QANA effectively integrates ghost modules, efficient channel attention, and squeeze-and-excitation blocks for robust feature representation with low-latency and energy-efficient inference. Its quantization-aware head and spike-compatible transformations enable seamless conversion to spiking neural networks (SNNs) and deployment on neuromorphic platforms. Evaluation on the large-scale HAM10000 benchmark and a real-world clinical dataset shows that QANA achieves 91.6% Top-1 accuracy and 82.4% macro F1 on HAM10000, and 90.8% Top-1 accuracy and 81.7% macro F1 on the clinical dataset, consistently outperforming leading CNN-to-SNN models under fair comparison. Deployed on BrainChip Akida hardware, QANA achieves 1.5 ms inference latency and 1.7 mJ energy per image, reducing inference latency and energy use by over 94.6%/98.6% compared to GPU-based CNNs, and exceeding the performance of advanced CNN-to-SNN conversion methods. These results demonstrate the effectiveness of QANA for accurate, real-time, and privacy-sensitive medical analysis in edge environments.

Index Terms—Resource-Constrained Devices, Edge Computing, Skin Disease Classification, Low Latency, Energy Efficiency

I. INTRODUCTION

Skin diseases present significant diagnostic challenges, particularly for clinicians without specialized training, leading to frequent misdiagnosis of conditions such as melanoma and Merkel cell carcinoma [1], [2]. Although deep learning-based diagnostic systems have shown promising performance [3], most approaches rely on centralized training and inference, requiring sensitive patient data to be transferred to cloud

Haitian Wang, Xinyu Wang, Yiren Wang, Zichen Geng, and Xian Zhang are with the Department of Computer Science and Software Engineering, The University of Western Australia, 35 Stirling Hwy, Crawley 6009, Western Australia, Australia. E-mail: haitian.wang@uwa.edu.au; xinyu.wang@uwa.edu.au; bohr.wang@uwa.edu.au; zen.geng@research.uwa.edu.au; xian.zhang @research.uwa.edu.au.

Yu Zhang (Corresponding author) is with the School of Computer Science, Northwestern Polytechnical University, Chang'an District, Xi'an, Shaanxi 710129, China. E-mail: zhangyu@nwpu.edu.cn.

Bo Miao is with the Australian Institute for Machine Learning (AIML), The University of Adelaide, Adelaide, SA 5005, Australia. E-mail: bo.miao@adelaide.edu.au.

servers [4]. This raises data security risks [5] and is constrained by strict privacy regulations such as HIPAA [6] and GDPR [7]. Furthermore, to support dermatological care in home and remote settings lacking conventional healthcare infrastructure [8], it is essential to develop models that enable on-device training and inference.

However, deploying deep learning models on edge devices faces several challenges. Conventional CNNs require significant computational and energy resources, increasing device complexity and limiting portability [9]. In addition, effective training typically depends on large labeled datasets, which are often unavailable for rare skin diseases [10], [11]. Frequent model updates further introduce computational overhead and privacy concerns, while hardware constraints restrict model complexity and inference accuracy on edge platforms [2].

Recently, Spiking Neural Networks (SNNs) and neuromorphic computing platforms have emerged as promising alternatives for overcoming deployment challenges in dermatological diagnosis [12]. Unlike conventional CNNs, SNNs use discrete spike events for information encoding and transmission, resulting in sparse and event-driven computation that greatly reduces power consumption [13]. This spike-based encoding is well-suited for scenarios with limited labeled data, as the temporal dynamics of spikes facilitate effective learning from fewer examples [14]. Neuromorphic processors, such as BrainChip's Akida [15], IBM's TrueNorth [16], and Intel's Loihi [17], natively support SNNs and enable on-chip incremental learning. Incremental learning enables these systems to adapt efficiently to new patient data without full model retraining, aligning well with clinical practices that regularly acquire new diagnostic cases [18]. Additionally, these neuromorphic devices possess compact physical footprints and substantially lower energy requirements compared to conventional GPUs [19], making them viable candidates for edge-based deployment in portable diagnostic instruments.

The prevalent approach for neuromorphic deployment is to first train conventional CNN architectures, such as ResNet or DenseNet, on large datasets, and then convert them to equivalent SNN models for edge inference [20]. While this conversion aims to combine the accuracy of CNNs with the efficiency of SNNs [21], several practical limitations persist. Key CNN components, such as Batch Norm, Flatten, and Global Average Pooling, cannot be directly mapped to spike-based neuron units, complicating and often degrading the conversion process [22]. In addition, converted SNNs frequently experience significant accuracy loss on small, imbalanced medical

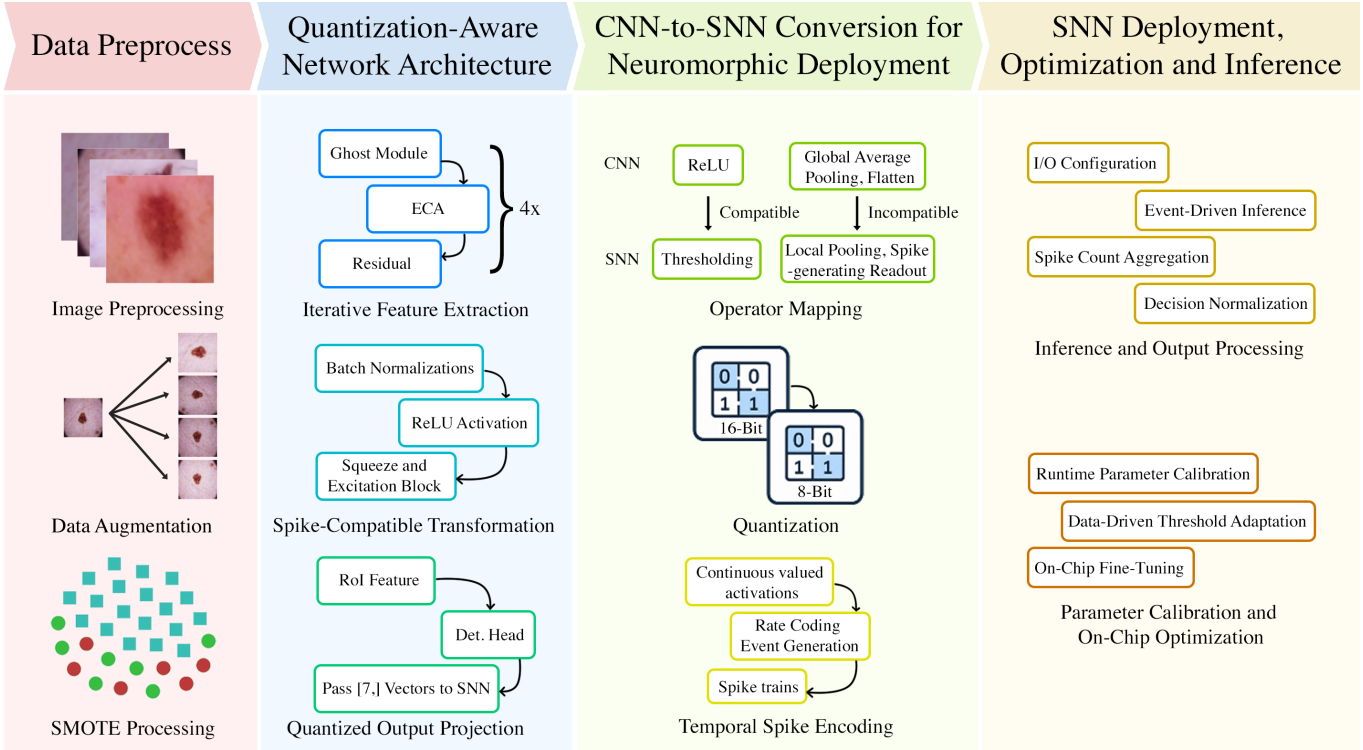


Fig. 1. Detailed architecture of our end-to-end framework for quantization-aware neuromorphic skin lesion classification: (1) data preprocessing (quality filtering, augmentation, and SMOTE-based oversampling); (2) a novel quantization-aware network for feature extraction and spike-compatible transformation; (3) CNN-to-SNN conversion with operator mapping and temporal spike encoding; and (4) SNN deployment with on-chip optimization for real-time and energy-efficient inference on edge hardware.

datasets due to quantization effects and limited capacity for capturing subtle pathological features [23].

We propose a quantization-aware neuromorphic architecture (QANA) within an end-to-end pipeline (Fig. 1) to overcome these challenges. QANA comprises three essential modules: (1) iterative feature extraction and downsampling block utilizing stacked Ghost modules, spatially-aware efficient channel attention (SA-ECA), and residual connections to reduce computation and inference latency, thereby directly facilitating effective CNN-to-SNN conversion; (2) spike-compatible feature transformation block employing quantization-aware normalization, bounded activations, and squeeze-and-excitation (SE) blocks, ensuring hardware compatibility and efficient incremental learning; and (3) quantized output projection block explicitly optimized for conversion-preserving CNN-to-SNN mapping and low-power neuromorphic deployment. These components collectively address key conversion limitations, preserve high accuracy for rare diseases, and efficiently support incremental model updates on edge devices.

Evaluations on the HAM10000 benchmark dataset show that QANA achieves a Top-1 accuracy of 91.6% and a macro F1 score of 82.4%. Further validation on a clinical dataset confirms robustness, achieving a Top-1 accuracy of 90.8% and a macro F1 score of 81.7%. When deployed on the Akida neuromorphic hardware platform, QANA attains an inference latency of 1.5 ms per image and energy consumption of 1.7 mJ, reducing inference latency and energy use by over 94.6%/98.6% compared to GPU-based CNNs, surpassing state-of-the-art CNN-to-SNN conversion methods in computational efficiency. These outcomes verify QANA's practical

suitability for resource-constrained and privacy-sensitive medical diagnostic applications.

Our main contributions are:

- *Conversion-preserving architecture.* We design QANA with bounded activations, separable and ghost convolutions, and lightweight channel attention with SE gating, ensuring all operators lower one-to-one to 8-bit spiking kernels.
- *Deployment-aligned training and conversion.* We provide a graph-preserving flow with batch-norm fusion and affine 8-bit quantization, combined with QAT, embedding-space SMOTE with safety filtering, and a lightweight on-chip incremental readout update, all under a fixed 64×64 input and matched preprocessing.
- *Edge evaluation.* On Akida and under identical preprocessing and quantization for baselines, QANA achieves 91.6% Top-1 and 82.4% macro F1 on HAM10000 and 90.8%/81.7% on a clinical set, with 1.5 ms latency and 1.7 mJ per image.

II. RELATED WORK

This section surveys the landscape for edge dermatology. We first outline neuromorphic hardware capabilities and constraints that govern feasible model design. We then compare ANN-to-SNN conversion with direct SNN training, including spike encoding and sparsity control, and finally review CNN-based dermatology systems as accuracy baselines. Across these threads we emphasize limitations under small and imbalanced datasets and strict latency and energy budgets, which together define the problem setting.

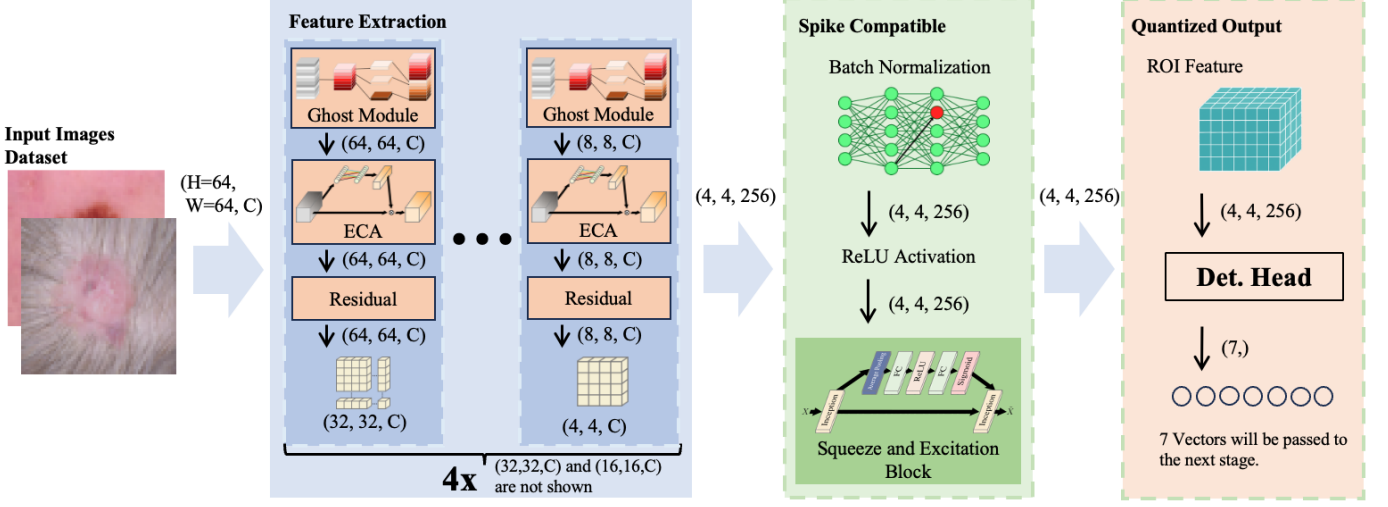


Fig. 2. Detailed architecture of our QANA, which performs iterative feature extraction using stacked Ghost modules, ECA, and residual blocks, followed by spike-compatible transformation with batch normalization, ReLU activation, and Squeeze-and-Excitation (SE) block. The output is then quantized and projected to class logits for SNN deployment.

A. Neuromorphic Hardware for Edge Imaging

Neuromorphic processors execute event-driven computation with low power and support on-chip adaptation, which matches the requirements of on-device medical imaging [14]. Akida, TrueNorth, and Loihi provide hardware support for spiking inference and incremental learning [15]–[17]. At the same time, these platforms constrain model design through limited operator sets, fixed-point quantization, and resource budgets that restrict input resolution and intermediate state. Related methods must therefore account for quantization and operator compatibility during both training and deployment.

B. ANN-to-SNN Conversion

A prevalent strategy trains a conventional CNN and converts it to an SNN by mapping activations to spikes with calibrated thresholds and quantized ranges [24]. Conversion enables reuse of mature backbones but introduces several sources of error. Batch normalization and global pooling do not admit direct spike-based equivalents, which forces structural edits and alters feature statistics. Rate-coded readouts require temporal integration that increases latency and makes predictions sensitive to threshold and timestep calibration, which is difficult to tune on small and imbalanced datasets. Empirical studies report measurable accuracy drops after conversion under these conditions, indicating that quantization and operator mismatch are primary failure modes on edge workloads [15].

C. Directly Trained SNNs and Spike Encoding

Direct training replaces the non-differentiable spike with surrogate derivatives and optimizes spiking dynamics end-to-end. SLAYER derives a time-domain error assignment rule for convolutional SNNs with learnable delays [25], and surrogate-gradient frameworks formalize stable optimization for deep networks [26]. Subsequent work improves few-timestep accuracy with residual spiking blocks [27] and temporal efficient training that couples the loss across discrete integration steps [28]. Despite these advances, training remains sensitive to

surrogate choice, thresholds, and timestep schedules. Performance depends on spike encoding. Time-to-first-spike and related temporal codes reduce spikes and latency [29], [30], yet they complicate calibration on hardware designed for rate accumulation and may reduce robustness on fine-grained classes when data are scarce. Activity regularization controls event rates and energy [25], [31], but aggressive sparsity can underfit rare patterns. These factors make it difficult to guarantee accuracy, latency, and energy simultaneously under fixed hardware constraints.

D. CNN-Based Dermatology Models

Dermatology classifiers based on DenseNet-121 and Inception-v4 reach strong results on ISIC-style datasets [32], [33]. In practice, deployment often depends on cloud retraining to handle distribution shift and rare categories, which introduces latency and privacy risk [18], [34]. Training data are class-imbalanced and images vary across devices and skin tones, which limits generalization to underrepresented conditions [35]. These limitations indicate that comparative evaluation on edge hardware should consider both conversion-based pipelines and directly trained SNNs with temporal encodings and sparsity control, so that the impact of quantization, operator compatibility, and encoding choices on accuracy, latency, and energy can be isolated under identical deployment settings.

III. METHODOLOGY

This section details the complete pipeline for the development and deployment of the proposed neuromorphic skin lesion classification system. As shown in Fig. 1, the pipeline encompasses data preprocessing, the design of a quantization-aware neural network architecture compatible with spiking inference, conversion to an event-driven SNN format, and hardware-level deployment on the Akida platform.

A. Data Preprocessing

The pipeline includes three main stages: image preprocessing to ensure quality and compatibility with the Akida

hardware, data augmentation to enhance dataset diversity and robustness, and SMOTE to address severe class imbalance among lesion categories.

1) *Image Preprocessing*: All dermatoscopic images undergo automated integrity checks followed by a brief manual review when needed. Inputs are processed at 64×64 to match the Akida on-chip memory budget used in our deployment. To retain lesion content at this resolution, we apply Grad-CAM on the pretrained backbone to obtain a coarse saliency map. A tight square crop is centered on the top-activated region and resized with antialiased area resampling to 64×64 . If the saliency peak lies within 10% of the image center or the saliency map is flat (coefficient of variation < 0.05), we fall back to a centered square crop. Pixel intensities are normalized per channel to $[0, 1]$. No denoising or inpainting is used.

2) *Data Augmentation*: Augmentations preserve dermoscopic color cues. We use random horizontal and vertical flips (probability 0.5). Luminance is perturbed on the CIELAB L channel with a multiplicative factor in $[0.95, 1.05]$ or a gamma factor in $[0.97, 1.03]$. Contrast is adjusted in $[0.95, 1.05]$. No hue shift is applied. A gray-world normalization fitted on the training split is used during training only. All random draws use fixed seeds for reproducibility.

3) *Synthetic Minority Oversampling (SMOTE)*: We perform SMOTE strictly in the learned embedding space rather than on raw pixels. For each training image x_i from class c , the backbone and spike-compatible transform produce a penultimate representation $\mathbf{r}_i \in \mathbb{R}^{4096}$ after global flattening. Let \mathcal{I}_c be the index set of class c and $\{\mathbf{r}_i\}_{i \in \mathcal{I}_c}$ the corresponding embeddings. Before neighbor search, embeddings are standardized on the *training split only* to avoid information leakage. A PCA whitening is then fitted on the same split and applied to stabilize distances in high dimension. Writing the sample covariance as $\Sigma = \mathbf{U}\Lambda\mathbf{U}^\top$ and retaining the top $d = 256$ components, the whitened vector is

$$\tilde{\mathbf{r}}_i = \Lambda_d^{-\frac{1}{2}} \mathbf{U}_d^\top (\mathbf{r}_i - \boldsymbol{\mu}), \quad (1)$$

where $\boldsymbol{\mu}$ is the training mean, $\mathbf{U}_d \in \mathbb{R}^{4096 \times d}$ the leading eigenvectors and $\Lambda_d \in \mathbb{R}^{d \times d}$ their eigenvalues. Nearest neighbors are computed with Euclidean distance in the whitened space; for each $i \in \mathcal{I}_c$ we form a k -NN set \mathcal{N}_i with $k = 5$.

To reduce the influence of outliers, we keep only “safe” minority anchors whose local median neighbor distance is below the class-specific 90th percentile:

$$\begin{aligned} \mathcal{S}_c^{\text{safe}} &= \left\{ i \in \mathcal{I}_c \mid \text{med}_{j \in \mathcal{N}_i} \|\tilde{\mathbf{r}}_i - \tilde{\mathbf{r}}_j\|_2 \right. \\ &\quad \left. \leq Q_{0.9} \left(\left\{ \text{med}_{j \in \mathcal{N}_u} \|\tilde{\mathbf{r}}_u - \tilde{\mathbf{r}}_j\|_2 \right\}_{u \in \mathcal{I}_c} \right) \right\}. \end{aligned} \quad (2)$$

For each minority class c with $N_c = |\mathcal{I}_c|$ and $N_{\max} = \max_{c'} N_{c'}$, we synthesize to a target level τN_{\max} with $\tau = 0.85$ to avoid distribution collapse. The number of synthetic embeddings is

$$M_c = \max(0, \lfloor \tau N_{\max} - N_c \rfloor). \quad (3)$$

Each synthetic vector is generated from an anchor $i \in \mathcal{S}_c^{\text{safe}}$ and a random neighbor $j \in \mathcal{N}_i$ by a convex interpolation and a small, locally aligned perturbation to improve diversity. Let \mathbf{C}_i be the empirical covariance of $\{\tilde{\mathbf{r}}_u\}_{u \in \{i\} \cup \mathcal{N}_i}$, and let $\mathbf{U}_i^{(m)}$ contain its $m = 8$ principal directions. With

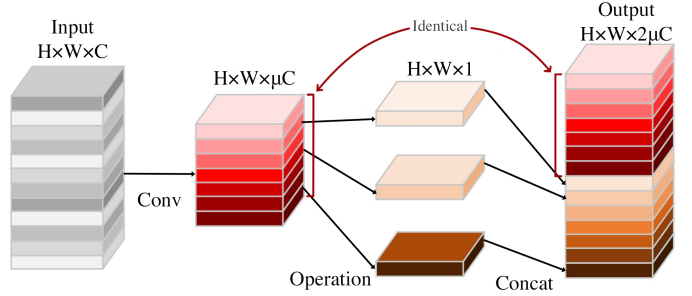


Fig. 3. Schematic of the Ghost module. The input feature map is first processed by a lightweight convolution to extract a reduced set of primary features with channel size μC , where C is the target output dimensionality and $\mu \in (0, 1)$ is a tunable ratio. Subsequently, inexpensive operations are applied to the primary features to generate additional ghost features of size $(1 - \mu)C$. These are concatenated along the channel axis to form the final output of size C .

$\delta_i = \text{med}_{j \in \mathcal{N}_i} \|\tilde{\mathbf{r}}_i - \tilde{\mathbf{r}}_j\|_2$ and $\sigma_c = 0.05 \text{ med}_{u \in \mathcal{I}_c} \delta_u$, we sample

$$\tilde{\mathbf{r}}_{\text{new}} = \tilde{\mathbf{r}}_i + \eta(\tilde{\mathbf{r}}_j - \tilde{\mathbf{r}}_i) + \sigma_c \mathbf{U}_i^{(m)} \boldsymbol{\xi}, \quad \eta \sim \mathcal{U}(0, 1), \quad \boldsymbol{\xi} \sim \mathcal{N}(\mathbf{0}, \mathbf{I}_m). \quad (4)$$

The synthetic embedding is then mapped back to the original feature space by the inverse whitening:

$$\mathbf{r}_{\text{new}} = \boldsymbol{\mu} + \mathbf{U}_d \Lambda_d^{\frac{1}{2}} \tilde{\mathbf{r}}_{\text{new}}. \quad (5)$$

Synthetic data are *not* images. They are injected at the penultimate layer as additional feature vectors and used to train the quantized output projection with cross-entropy. During this stage the backbone up to the spike-compatible transform is frozen; only the classifier head is updated for 5 epochs with mixed real and synthetic embeddings. A subsequent short fine-tuning on real data only re-enables the last block and the head to reconcile the feature distribution. Input images are still resized to 64×64 prior to feature extraction for hardware constraints, but no pixel-space mixing or image synthesis is performed at any time.

B. Quantization-Aware Network Architecture

The model (as shown in Fig. 2) comprises a hierarchical cascade of Ghost-based multi-scale feature extraction blocks, integrated channel attention mechanisms, and a quantization-aware transformation stage that produces SNN-ready outputs. This architecture balances computational efficiency and discriminative power, facilitating direct conversion and robust inference on the Akida neuromorphic platform.

1) *Iterative Feature Extraction and Downsampling*: Feature extraction begins with a stack of Ghost blocks [36], designed to maximize representational diversity while minimizing computational cost. As shown in Fig. 3, each Ghost block receives a feature tensor $F^{(l-1)}$ (for $l = 1, \dots, 4$) and applies both base and ghost convolutions as:

$$F_{\text{ghost}}^{(l)} = \text{Concat} \left(\underbrace{\mathcal{F}_{1 \times 1}^{(l)}(F^{(l-1)})}_{\text{base: pointwise conv}}, \underbrace{\mathcal{F}_{3 \times 3}^{(l)}(F^{(l-1)}) \odot \mathbf{M}^{(l)}}_{\text{ghost: depthwise conv with filter mask}} \right) \quad (6)$$

Here, $\mathcal{F}_{k \times k}^{(l)}$ is a separable convolution of kernel size $k \times k$, and $\mathbf{M}^{(l)}$ is a binary mask selecting learnable ghost filters. This combination generates both local and extended receptive fields, enabling richer features with fewer FLOPs.

After concatenation, the tensor is processed by batch normalization, quantization-bounded activation, and dropout:

$$F_{\text{drop}}^{(l)} = \text{Dropout} \left(\min(6, \max(0, \gamma^{(l)} \cdot \text{BN}(F_{\text{ghost}}^{(l)}) + \beta^{(l)})) \right) \quad (7)$$

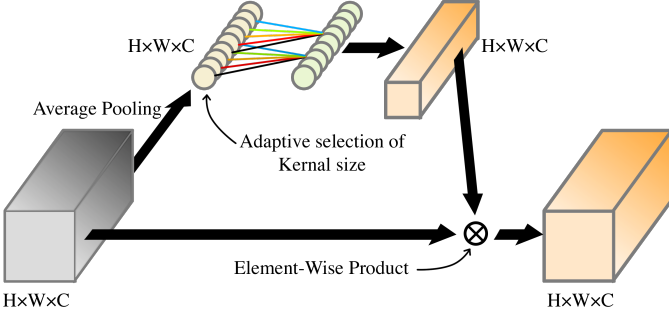


Fig. 4. Illustration of the Spatially-Aware ECA (SA-ECA) block. A depthwise convolution is first applied to extract channel-wise statistics, followed by a lightweight 1D convolution to model local channel dependencies. The resulting attention weights are used to rescale the input feature channels, enhancing discriminative information with minimal computational overhead.

This quantization-aware step is crucial for downstream SNN compatibility and robust generalization.

To capture cross-channel correlations, each block integrates a Spatially-Aware Efficient Channel Attention (SA-ECA) mechanism, inspired by Efficient Channel Attention (ECA) mechanism [37]. As shown in Fig. 4, Instead of computing global channel statistics via global average pooling and 1D convolution, we adopt a lightweight depthwise convolution followed by pointwise channel-wise scaling. This enables efficient modeling of spatial-channel dependencies with minimal overhead and neuromorphic compatibility:

$$\tilde{F}^{(l)} = \sigma \left(\mathbf{W}_{1 \times 1}^{(l)} * \text{BN} \left(\text{DWConv}_{k \times k} \left(F^{(l)} \right) \right) \right) \odot F^{(l)} \quad (8)$$

where $\text{DWConv}_{k \times k}$ and $\mathbf{W}_{1 \times 1}^{(l)}$ jointly form the attention mechanism in our SA-ECA block, and σ is the sigmoid activation used to generate the attention mask. This lightweight attention preserves channel expressiveness with minimal overhead.

To ensure stable deep stacking, we employ residual skip connections and spatial downsampling:

$$F^{(l)} = \text{MaxPool2D} \left(\alpha^{(l)} \odot F_{\text{drop}}^{(l)} + \mathbf{P}^{(l)} F^{(l-1)} \right) \quad (9)$$

where $\mathbf{P}^{(l)}$ projects the previous block's output for dimension alignment if needed. This design preserves gradient flow, reduces vanishing/exploding risk, and aggregates multi-scale context, all critical for reliable feature extraction in small-data regimes. After four such blocks, the spatial size is reduced to 4×4 .

2) *Spike-Compatible Feature Transformation*: The output of the previous stage, $F^{(4)}$, is passed to a spike-compatible transformation module engineered for direct quantization and SNN integration. A SeparableConv2D ($3 \times 3, 256$) [38] generates higher-dimensional features, followed by quantization-aware normalization and bounded activation:

$$\hat{F} = \min \left(6, \max \left(0, \gamma_{\text{spk}} \cdot \text{BN}(\text{SepConv}_{3 \times 3, 256}(F^{(4)})) + \beta_{\text{spk}} \right) \right) \quad (10)$$

This mapping guarantees that all activations lie in $[0, 1]$, which is both compatible with spike encoding and preserves information for subsequent inference.

To further optimize the channel-wise information flow, as shown in Fig. 5, a Squeeze-and-Excitation (SE) block [39] is applied, implementing a two-stage bottleneck and gating mechanism:

$$\mathbf{s} = \sigma \left(W_2 \delta \left(W_1 \frac{1}{16} \sum_{i,j} \hat{F}(i,j,:) \right) \right) \quad (11)$$

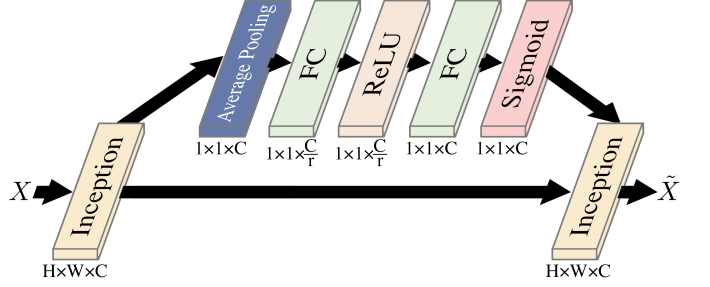


Fig. 5. Illustration of the Squeeze-and-Excitation (SE) block. The input feature map undergoes global pooling, followed by two fully connected layers with ReLU and sigmoid activations to compute channel-wise weights. The original feature map is then rescaled by these weights, enabling adaptive recalibration of channel responses.

where W_1 and W_2 are dense layers, δ is ReLU, and σ is sigmoid. Each feature channel is then scaled by s_c , which adaptively modulates discriminative capacity and provides additional regularization for small, imbalanced datasets.

3) *Quantized Output Projection*: The final block flattens the spike-compatible features \hat{F} to a vector $r \in \mathbb{R}^{4096}$ and applies a linear projection to produce the model output:

$$\mathbf{y} = \mathbf{W}_{\text{cls}} r + \mathbf{b}_{\text{cls}} \quad (12)$$

Here, $\mathbf{W}_{\text{cls}} \in \mathbb{R}^{7 \times 4096}$, $\mathbf{b}_{\text{cls}} \in \mathbb{R}^7$. The output \mathbf{y} is a 7-dimensional, already quantized vector that can be seamlessly passed to the SNN converter for neuromorphic inference.

C. CNN-to-SNN Conversion for Neuromorphic Deployment

We convert the trained quantization-aware CNN to an event-driven SNN using a graph-preserving flow with three stages: static reparameterization, integer quantization with calibration or QAT, and hardware-constrained code generation. First, all Batch Normalization layers are eliminated by fusing their affine statistics into the preceding convolution or pointwise projection. For a convolution output channel c with kernel \mathbf{W}_c and bias b_c and BN parameters $(\gamma_c, \beta_c, \mu_c, \sigma_c^2, \epsilon)$, the fused weights and bias are

$$\mathbf{W}'_c = \frac{\gamma_c}{\sqrt{\sigma_c^2 + \epsilon}} \mathbf{W}_c, \quad b'_c = \frac{\gamma_c}{\sqrt{\sigma_c^2 + \epsilon}} (b_c - \mu_c) + \beta_c. \quad (13)$$

Depthwise and separable convolutions are treated identically channel-wise. Nonlinearities not in the target activation set are replaced during training by bounded ReLU6 so that all post-activation tensors are in $[0, 6]$, which simplifies downstream spike generation and avoids undefined mappings in the spiking domain [24], [40]. Global average pooling is lowered to an integer spatial reduction with compile-time division embedded in the output scale. Flatten is treated as a metadata reshape and does not generate compute kernels. Softmax is applied on the host side after spike integration [24].

Quantization follows an affine, per-tensor, uniform scheme for both weights and activations with 8-bit fixed-point. Let a denote a real activation and (s_a, z_a) the scale and zero-point obtained by calibration on a held-out set or learned with quantization-aware training. The integer activation and its error are

$$a_q = \text{clip} \left(\text{round} \left(\frac{a}{s_a} \right) + z_a, 0, 255 \right), \quad e_a = a - (a_q - z_a) s_a. \quad (14)$$

During SNN emission, each neuron integrates the quantized drive and generates a binary event whenever the internal accumulator crosses a programmable threshold τ ; resetting

is subtractive. With state u_t and drive a_q the discrete-time dynamics are

$$s_t = \mathbb{I}(u_{t-1} + a_q \geq \tau), \quad u_t = (u_{t-1} + a_q) - \tau s_t, \quad (15)$$

and rate readout uses the spike count within an integration window. For ReLU6, $s_a = 255/6$ and $z_a = 0$ make the activation-range utilization explicit and fix the time-to-first spike under a given τ [24].

Operator lowering is rule-based and deterministic. Convolution, depthwise convolution, separable convolution, average pooling, max pooling, elementwise clipping and integer linear layers are mapped one-to-one to supported spiking kernels. Global average pooling is lowered to an integer spatial reduction with compile-time division by the pooling area embedded in the output scale. Flatten is a metadata reshape that preserves memory layout and does not generate compute kernels. Unsupported nonlinearities such as Swish or hard-Swish are removed at training time and replaced by ReLU6. Squeeze-and-Excitation is realized by keeping the global pooling and two low-rank linear projections in the quantized graph and folding the final channel-wise gating into the subsequent pointwise projection when possible, otherwise emitting a per-channel integer rescale. Residual additions are integer tensor adds after scale alignment by rational multipliers that are absorbed into the successor scale. The converter rejects any subgraph that would require a floating-point dequantize. To make the comparison across backbones fair, a model is deemed *convertible* only if the compiled spiking graph contains no dequantize fallback and every tensor is quantized to 8-bit throughout the feature extraction and readout path; otherwise the model is excluded from neuromorphic evaluation and reported as a failed conversion.

Fairness metrics and logs are computed on the same train and test splits and under identical preprocessing. We retrain each CNN baseline with the same input resolution, the same augmentation policy, the same learning-rate schedule, and the same 8-bit quantization configuration, then convert and deploy the resulting SNN. Conversion success rate is defined on the quantized graph \mathcal{G} as

$$r_{\text{succ}} = 1 - \frac{|\mathcal{V}_{\text{fp32}}|}{|\mathcal{V}|}, \quad (16)$$

where \mathcal{V} is the node set and $\mathcal{V}_{\text{fp32}}$ are nodes that would require dequantization and thus cannot be placed on the neuromorphic cores. Accuracy drop is reported as $\Delta\text{Acc} = \text{Acc}_{\text{SNN}} - \text{Acc}_{\text{CNN}}$ and $\Delta\text{F1} = \text{F1}_{\text{SNN}} - \text{F1}_{\text{CNN}}$ on the same test set. For transparency, we release per-model conversion manifests listing, for every layer, the integer scale and zero-point, the applied reparameterization, and the final kernel selected by the code generator. The mapping rules in (13)–(16) and the practice of bounded activations to guarantee spike-compatibility follow established CNN-to-SNN conversion principles and 8-bit QAT literature.

D. SNN Deployment, Optimization and Inference

The converted SNN model is deployed directly onto the BrainChip Akida neuromorphic processor for hardware-based inference. The deployment process comprises several steps:

loading the SNN model into the hardware runtime environment, configuring input/output data streams, and initializing internal buffers and neuron state registers.

1) *Inference and Output Processing*: Inference is performed in an event-driven manner, with input images encoded into spike trains and propagated through the SNN in a fully parallel fashion. For each test or validation sample, the model outputs spike counts or firing rates at the final output neurons, corresponding to the target classes. To robustly map temporal spike responses to class probabilities, we aggregate the spike counts $S_c(t)$ for each class c within an integration window T , and apply a soft decision normalization:

$$\hat{p}_c = \frac{\exp\left(\alpha \sum_{t=1}^T w_t S_c(t)\right)}{\sum_{k=1}^C \exp\left(\alpha \sum_{t=1}^T w_t S_k(t)\right)} \quad (17)$$

where w_t is an optional temporal weighting factor (e.g., $w_t = \exp(-\beta(T-t))$ for decaying integration), α is a scaling parameter, and C is the number of output classes. Class prediction is then made as $\arg \max_c \hat{p}_c$.

2) *Parameter Calibration and On-Chip Optimization*: After initial deployment, key runtime parameters—such as output spike thresholds, integration windows, and temporal pooling parameters—are empirically calibrated on a held-out validation set. To further optimize the class assignment and suppress spurious events, a threshold adaptation can be formulated as:

$$\theta_c^* = \arg \min_{\theta} \left\{ \sum_{i=1}^N \mathbb{I}[y_i \neq \mathbb{I}(S_c^{(i)} > \theta)] \right\} \quad (18)$$

where $S_c^{(i)}$ is the total spike count for class c on sample i , y_i is the true label, and $\mathbb{I}[\cdot]$ is the indicator function. This allows data-driven threshold selection for each class. If performance deviation is observed relative to the original CNN, light on-chip fine-tuning is conducted using Akida's incremental learning capability, adjusting only the last output layer to optimize for domain shift or quantization artifacts. For higher-detail cases, a 2×2 tiling fallback is triggered when $\max_c \hat{p}_c < 0.60$. Four overlapping 64×64 patches (20% stride overlap) are evaluated and logits averaged. On HAM10000, the trigger rate is 18%.

IV. EXPERIMENT

This section presents the datasets, experimental setup, and evaluation protocols, followed by detailed quantitative analyses of classification performance, ablation studies, and efficiency metrics under various deployment conditions.

A. Datasets

We used two datasets: the public HAM10000 benchmark and a proprietary clinical dataset from local hospital. Both sets reflect a range of lesion types and clinical diversity.

1) *HAM10000 Dataset*: The HAM10000 dataset [41] consists of 10,015 dermatoscopic RGB images labeled by expert dermatologists into seven categories: melanocytic nevus, melanoma, benign keratosis-like lesions, basal cell carcinoma, actinic keratosis/intraepithelial carcinoma, vascular lesions, and dermatofibroma. The images originate from diverse sources and exhibit significant class imbalance. For all experiments, we adopted a standard 70%/10%/20% train/validation/test split.

TABLE I

CLASS-WISE PRECISION, RECALL, F1, AND PER-CLASS ACCURACY ON THE HAM10000 TEST SET. THE MACRO F1 EQUALS THE UNWEIGHTED MEAN OF PER-CLASS F1.

Class	Precision	Recall	F1	Accuracy
Actinic keratoses	0.840	0.820	0.830	0.820
Basal cell carcinoma	0.830	0.820	0.820	0.820
Benign keratosis-like	0.800	0.780	0.790	0.780
Dermatofibroma	0.900	0.860	0.880	0.860
Melanocytic nevi	0.800	0.740	0.770	0.740
Vascular lesions	0.870	0.850	0.860	0.850
Melanoma	0.830	0.810	0.820	0.810
Macro average	0.853	0.826	0.824	0.826

2) *local Clinical Dataset*: A non-public clinical dermatoscopic dataset was provided by a partner hospital under a data-use agreement. The dataset comprises 3,162 images from 1,835 patients acquired during routine care between June 2022 and February 2024. No human experiments or prospective data collection were conducted by the authors. Lesion categories were harmonized to the seven HAM10000 classes; rare or unclassified cases were excluded to maintain consistent labeling. Each case was independently annotated by at least two board-certified dermatologists, with histopathology confirmation when available. All records were de-identified before access and used solely for secondary analysis. Dataset partitioning followed the same 70%/10%/20% train/validation/test split as HAM10000, stratified by disease category, providing a clinically diverse, real-world validation source for model generalization.

B. Experimental Setup

All training and conversion are performed on a workstation with an Intel Core i9-12900K CPU, 128 GB RAM, and an NVIDIA RTX 3090, running Ubuntu 22.04 LTS. Software includes Python 3.9, CUDA 11.8, TensorFlow 2.10, and Akida MetaTF SDK v2.2.1. Unless otherwise stated, batch size is 1 for latency and energy measurement. We use AdamW (weight decay 10^{-4}), initial learning rate 3×10^{-4} with cosine decay for 120 epochs, and early stopping on validation macro F1. Quantization-aware training uses 8-bit affine per-tensor quantization for weights and activations with ReLU6 clipping. Neuromorphic inference uses a BrainChip Akida AKD1000 PCIe board with default runtime settings. GPU energy is measured as the board power above idle (averaged by NVML at 20 Hz) multiplied by the per-image inference time; Akida energy is measured analogously by on-board power monitoring. Reported Akida 1.5 ms corresponds to on-chip execution time; host preprocessing and I/O add < 0.2 ms on average and are reported separately when stated.

C. Analysis of Classification Results on HAM10000 Dataset

Table I reports per-class precision, recall, F1, and per-class accuracy under the 64×64 single-pass setting. The macro F1 is 0.824. Vascular lesions ($F1 = 0.860$) and dermatofibroma ($F1 = 0.880$) rank highest, whereas benign keratosis-like lesions ($F1 = 0.790$) and melanocytic nevi ($F1 = 0.770$) are lower, consistent with known visual overlap between these categories and class imbalance in the dataset. Errors are concentrated between nevi and benign keratosis-like lesions and at the nevi–melanoma boundary. The channel reweighting modules (ECA/SE) suppress redundant responses and improve

TABLE II
PERFORMANCE COMPARISON OF CONVERTED SNN MODELS ON HAM10000

Model (SNN, Akida)	Top-1 Accuracy (%)	Macro F1 (%)
ResNet-50 [9]	85.7	76.4
DenseNet-121 [32]	86.5	77.2
Inception-v4 [33]	85.9	76.9
EfficientNet-B4 [42]	87.3	78.1
MobileNet-v2 [43]	83.4	74.7
SENet-154 [44]	86.9	77.8
Xception [11]	85.5	76.2
Multi-Scale Attention [35]	87.0	78.0
CNN Ensemble [45]	88.1	78.9
AKIDANet [15]	83.2	73.6
Ours	91.6	82.4

minority coverage, which aligns with the relatively stronger performance in vascular lesions and dermatofibroma.

Per-class accuracy in the table largely mirrors recall by construction and is provided for completeness. All decisions use plain argmax without threshold tuning. The image-level Top-1 accuracy on the same test split is 91.6%, while the macro F1 remains more conservative due to equal weighting across classes.

D. Classification Performance on HAM10000

To comprehensively evaluate the effectiveness of our neuromorphic skin lesion classification system, we conducted a series of controlled experiments in which a selection of state-of-the-art convolutional neural network (CNN) architectures were converted to spiking neural networks (SNNs) using our quantization-aware pipeline and executed on the same Akida hardware platform. This strategy ensures a fair comparison of all approaches under identical hardware constraints and SNN deployment settings. The evaluated models include both canonical CNN baselines and advanced architectures commonly used in medical image analysis.

As shown in Table II, all evaluated CNN models show a decrease in accuracy and macro F1 score after conversion to SNN and deployment on neuromorphic hardware, with Top-1 accuracy values ranging from 83.2% to 88.1%. In contrast, our proposed model achieves a Top-1 accuracy of 91.6% and a macro F1 score of 82.4%, outperforming all baselines under the same SNN deployment conditions. This improvement demonstrates the benefit of our quantization-aware architecture and optimized network design for event-driven inference. The results confirm the practical utility of our method for real-time, resource-constrained medical applications, supporting efficient and accurate classification in portable diagnostic systems.

E. Inference Speed and Energy Consumption

We quantitatively evaluated the inference latency and energy consumption of our neuromorphic model in comparison with both conventional CNN baselines and other SNN-converted architectures. All SNN models were deployed on the Akida AKD1000 PCIe board, while CNN baselines were tested on both NVIDIA RTX 3090 GPU and an Intel Xeon CPU. For each model, the reported inference latency corresponds to the average per-image processing time over 1000 test samples. Energy consumption per image was measured as the mean device power during inference multiplied by the average

TABLE III

PER-IMAGE INFERENCE LATENCY AND ENERGY CONSUMPTION OF ALL MODELS ON THE HAM10000 TEST SET. CNN BASELINES ARE MEASURED ON AN NVIDIA RTX 3090 (GPU) AND INTEL XEON GOLD 6226R (CPU); SNNs ARE MEASURED ON BRAINCHIP AKIDA AKD1000. ALL VALUES ARE AVERAGED OVER 10,000 IMAGES. THE RIGHTMOST COLUMNS SHOW THE PERCENTAGE REDUCTION ACHIEVED BY SNNs ON AKIDA COMPARED TO THE CORRESPONDING CNN (GPU) VERSION.

Model	CNN (GPU)		CNN (CPU)		SNN (Akida)		Relative Reduction(%)	
	Latency (ms)	Energy (mJ)	Latency (ms)	Energy (mJ)	Latency (ms)	Energy (mJ)	Latency	Energy
ResNet-50 [9]	12.1	175.2	57.9	923.3	2.8	3.3	76.9	98.1
DenseNet-121 [32]	14.7	199.6	68.4	1075.2	3.1	3.5	78.9	98.2
Inception-v4 [33]	16.8	218.5	82.1	1237.5	3.5	4.1	79.2	98.1
EfficientNet-B4 [42]	18.9	242.1	93.6	1345.6	4.0	4.6	78.8	98.1
MobileNet-v2 [43]	6.9	97.5	68.2	1082.1	2.2	2.6	68.1	97.3
SENet-154 [44]	17.3	236.8	89.4	1312.4	3.8	4.4	78.0	98.1
Xception [11]	10.7	151.2	51.5	863.7	2.6	3.1	75.7	97.9
Multi-Scale Attention [35]	19.8	251.7	97.7	1391.5	4.2	5.0	78.8	98.0
CNN Ensemble [45]	36.1	450.5	157.2	2177.1	7.5	8.6	79.2	98.1
QANA (Ours)	27.6	163.1	83.9	841.5	1.5	1.7	94.6	98.6

TABLE IV

ABLATION STUDY OF CORE MODULES IN OUR MODEL ON THE HAM10000 TEST SET. METRICS ARE REPORTED AS PERCENTAGES (%). EACH ROW SHOWS THE INCREMENTAL ADDITION OF MODULES.

Configuration	Ghost Block	ECA	SE	Quant. Head	SMOTE	Inc. Learn	Accuracy	Recall	Precision	F1 Score	AUC-ROC
Baseline							74.1	71.4	71.9	71.6	77.3
+ Ghost Block	✓						72.3	70.2	70.0	70.6	70.9
+ ECA	✓	✓					88.7	85.8	87.2	86.5	90.7
+ SE	✓	✓	✓				89.8	87.7	88.1	87.8	91.5
+ Augmentation	✓	✓	✓	✓			90.4	88.1	89.1	88.6	92.1
+ SMOTE	✓	✓	✓	✓	✓		91.0	89.2	90.0	89.6	92.7
+ Incremental Learning	✓	✓	✓	✓	✓	✓	91.6	90.7	91.2	90.9	93.4

inference time, using on-board power monitoring for Akida and NVIDIA-smi for GPU and Intel RAPL for CPU.

To ensure a fair and hardware-consistent comparison, all tested CNN architectures were converted to SNNs using our pipeline before deployment on Akida. Table III presents a comprehensive summary of inference latency and energy consumption across all evaluated models and platforms, as well as the relative reduction of these metrics for SNNs on Akida compared to their CNN GPU and CPU implementations. Our neuromorphic model achieves the lowest inference latency and energy consumption of all evaluated architectures. When deployed as an SNN on the Akida platform, it completes classification in 1.5 ms per image and requires just 1.7 mJ, representing an 94.6% reduction in latency and over 98.6% reduction in energy compared to the equivalent CNN on GPU surpassing all other state-of-the-art CNN-to-SNN conversion baselines.

For images requiring higher spatial detail, the 2×2 tiling fallback increases latency and energy approximately in proportion to the number of patches while remaining within the power envelope of the edge platform. This fallback is applied conditionally based on a confidence threshold on the single-pass prediction and does not change the training protocol.

F. Ablation Study of Model Components

Table IV summarizes a stepwise ablation in which we start from a compact baseline and incrementally enable Ghost, ECA, SE, quantization-aware head with the same augmentation policy, embedding-space SMOTE, and on-chip incremental learning. All experiments use the same input resolution, optimizer, schedules, and 8-bit quantization configuration to

TABLE V
PERFORMANCE COMPARISON OF CONVERTED SNN MODELS ON THE CLINICAL DATASET.

Model (SNN, Akida)	Top-1 Accuracy (%)	Macro F1 (%)
ResNet-50 [9]	84.6	75.3
DenseNet-121 [32]	85.7	76.2
Inception-v4 [33]	85.2	75.8
EfficientNet-B4 [42]	86.3	77.0
MobileNet-v2 [43]	82.8	73.7
SENet-154 [44]	85.4	76.6
Xception [11]	84.2	74.8
Multi-Scale Attention [35]	86.5	77.2
CNN Ensemble [45]	87.6	78.1
AKIDANet [15]	81.9	71.5
Ours	90.8	81.7

isolate the effect of each component. Metrics are computed on the same test split.

The drop observed for “Baseline + Ghost” is expected under a strictly width-preserving replacement of standard convolutions by Ghost modules. Ghost generates a fraction of channels through inexpensive linear transforms of a reduced set of primary channels. When used alone and early in the stack, this reduces the number of learned base filters that directly capture fine dermatoscopic structures such as pigment networks, streaks, and globules. The cheap transforms introduce correlated feature maps that do not add discriminative power without a mechanism to suppress redundancy. Under 8-bit activation clipping, these correlated responses compress the effective dynamic range and make the batch-norm folding more sensitive to local contrast, which in turn degrades minority-class recall. The combination of early downsampling and reduced primary channels further limits high-frequency detail preserved from 64×64 inputs. As a result, the test accuracy decreases relative to the baseline when Ghost is

introduced in isolation.

Adding ECA recovers and surpasses the baseline by providing lightweight channel recalibration that suppresses redundant ghosted maps and reweights informative channels. The subsequent SE block contributes a complementary global channel prior that stabilizes inter-class boundaries and improves calibration. Enabling the quantization-aware head with the same augmentation policy improves the match between integer ranges at the readout and the upstream bounded activations, which tightens the loss landscape after BN folding. Injecting SMOTE in the embedding space raises coverage of minority manifolds without perturbing low-level image statistics and yields consistent gains in macro metrics. Finally, on-chip incremental learning adapts the last-stage parameters to post-conversion activation statistics and to the deployment data distribution, producing the highest accuracy and F1. We also observed that widening the primary branch of Ghost or delaying its use to later stages can mitigate the initial drop, but we kept the compact configuration to satisfy on-chip memory and latency constraints and relied on attention and calibration to recover accuracy.

G. Classification Performance on Clinical Dataset

We evaluated the proposed neuromorphic skin lesion classification system and several representative CNN architectures, all converted to SNNs and deployed on the Akida hardware platform. Table V presents the Top-1 accuracy and macro F1 score for each model under the same deployment conditions. Our model achieves the highest accuracy and macro F1 score among all tested methods, confirming its effectiveness and robustness for neuromorphic inference in clinical scenarios.

V. CONCLUSION

We presented QANA, a quantization-aware neuromorphic pipeline for skin lesion classification on edge hardware. Under a fixed 64×64 input and identical preprocessing across methods, QANA reaches 91.6% Top-1 and 82.4% macro F1 on HAM10000 and 90.8%/81.7% on a clinical dataset. The compiled SNN runs at 1.5 ms on chip and 1.7 mJ per image on Akida, measured as power above idle. These results indicate that conversion-preserving design and deployment-aware training enable accurate and efficient on-device dermatology inference.

VI. ACKNOWLEDGEMENT

This research was supported by the National Natural Science Foundation of China (Nos. 62172336 and 62032018). The authors gratefully acknowledge BrainChip Holdings Ltd. for providing technical support and the Akida AKD1000 hardware platform, whose powerful neuromorphic computing capabilities enabled strong performance of the SNN model. The authors also extend their appreciation to Dr. Atif Mansoor and his teams for their preliminary contributions to this research.

REFERENCES

- [1] M. Jilani *et al.*, “Recent advances in the clinical application of transferosomes for skin cancer management,” *Colloids Surf. B*, 2025.
- [2] M. Mortaja and S. Demehri, “Skin cancer prevention—recent advances and unmet challenges,” *Cancer Lett.*, 2023.
- [3] H. Bhatt *et al.*, “State-of-the-art machine learning techniques for melanoma skin cancer detection and classification: a comprehensive review,” *Intell. Med.*, 2023.
- [4] M. M. Yaqoob *et al.*, “Symmetry in privacy-based healthcare: A review of skin cancer detection and classification using federated learning,” *Symmetry*, 2023.
- [5] K. Kourou *et al.*, “Applied machine learning in cancer research: A systematic review for patient diagnosis, classification and prognosis,” *Comput. Struct. Biotechnol. J.*, 2021.
- [6] D. McGraw and K. D. Mandl, “Privacy protections to encourage use of health-relevant digital data in a learning health system,” *NPJ Digit. Med.*, 2021.
- [7] M. Kretschmer *et al.*, “Cookie banners and privacy policies: Measuring the impact of the gdpr on the web,” *ACM Trans. Web*, 2021.
- [8] M. Janda *et al.*, “Early detection of skin cancer in australia—current approaches and new opportunities,” *Public Health Res. Pract.*, 2022.
- [9] B. Koonce, “Resnet 50,” in *CNNs with Swift for TensorFlow*, 2021.
- [10] L. E. Hernandez *et al.*, “Merkel cell carcinoma: An updated review of pathogenesis, diagnosis, and treatment options,” *Dermatol. Ther.*, 2022.
- [11] F. Chollet, “Xception: Depthwise separable convolutions,” in *CVPR*, 2017.
- [12] Y. Nie *et al.*, “Recent advances in diagnosis of skin lesions using dermoscopic images based on deep learning,” *IEEE Access*, 2022.
- [13] J.-K. Han *et al.*, “A review of artificial spiking neuron devices for neural processing and sensing,” *Adv. Funct. Mater.*, 2022.
- [14] E. Kim and Y. Kim, “Exploring the potential of spiking neural networks in biomedical applications,” *Biomed. Eng. Lett.*, 2024.
- [15] E. Bråtman and L. Dow, “Neuromorphic medical image analysis at the edge: On-edge training with the akida brainchip,” 2023.
- [16] R. Borrà, “Neuromorphic computing: Bridging biological intelligence and artificial intelligence,” *Int. J. Eng. Adv. Technol.*, 2024.
- [17] R. Scrofano *et al.*, “Radiation test performance of the intel loihi neuromorphic processor,” in *IEEE SCC*, 2024.
- [18] G. Chen *et al.*, “On-chip incremental learning based on unsupervised stdp implementation,” in *IEEE AICAS*, 2024.
- [19] R. Islam *et al.*, “Device and materials requirements for neuromorphic computing,” *J. Phys. D*, 2019.
- [20] C. D. Schuman *et al.*, “Real-time evolution and deployment of neuromorphic computing at the edge,” in *IGSC*, 2021.
- [21] D. R. Muir and S. Sheik, “The road to commercial success for neuromorphic technologies,” *Nat. Commun.*, 2025.
- [22] Y. Kim *et al.*, “Beyond classification: Directly training spiking neural networks for semantic segmentation,” *Neuromorphic Comput. Eng.*, 2022.
- [23] Y. Hu *et al.*, “Fast-snn: Fast spiking neural network by converting quantized ann,” *IEEE TPAMI*, 2023.
- [24] B. Rueckauer, I. Lungu, Y. Hu, M. Pfeiffer, and S.-C. Liu, “Conversion of continuous-valued deep networks to spiking networks,” *Front. Neurosci.*, 2017.
- [25] S. B. Shrestha and G. Orchard, “Slayer: Spike layer error reassignment in time,” in *Advances in Neural Information Processing Systems*, 2018.
- [26] E. O. Neftci, H. Mostafa, and F. Zenke, “Surrogate gradient learning in spiking neural networks,” *Nature Machine Intelligence*, vol. 1, no. 1, pp. 86–96, 2019.
- [27] W. Fang, Z. Yu, Y. Chen, T. Masquelier, Y. Tian, and other authors, “Deep residual learning in spiking neural networks,” in *Advances in Neural Information Processing Systems*, 2021.
- [28] S. Deng, S. Gu, Y. Wu, and G. Li, “Temporal efficient training of spiking neural networks,” in *Advances in Neural Information Processing Systems*, 2022.
- [29] H. Mostafa, “Supervised learning based on temporal coding in deep spiking neural networks,” in *Advances in Neural Information Processing Systems*, 2017.
- [30] P. U. Diehl and M. Cook, “Fast-classifying, high-accuracy spiking deep networks using temporal coding,” in *International Joint Conference on Neural Networks*, 2015.
- [31] N. Rathi, G. Srinivasan, P. Panda, and K. Roy, “Diet-snn: Direct training of deep spiking neural networks for low-latency and energy-efficient inference,” in *IEEE/CVF Conference on Computer Vision and Pattern Recognition Workshops*, 2020.
- [32] M. Chhabra and R. Kumar, “A smart healthcare system based on densenet-121,” in *Mobile Radio Commun. 5G Netw.*, 2022.
- [33] C. Szegedy *et al.*, “Inception-v4, inception-resnet and the impact of residual connections,” in *AAAI*, 2017.
- [34] M. Moor *et al.*, “Foundation models for generalist medical artificial intelligence,” *Nature*, 2023.

- [35] J. Qin *et al.*, “Multi-scale attention network for image inpainting,” *CVIU*, 2021.
- [36] K. Han *et al.*, “Ghostnet: More features from cheap operations,” in *CVPR*, 2020.
- [37] Q. Wang *et al.*, “Eca-net: Efficient channel attention for deep cnns,” in *CVPR*, 2020.
- [38] N. Rajabi *et al.*, “A method for detecting and localizing open-circuit switch faults in mmcs using separable conv2d neural networks,” *IEEE Trans. Ind. Electron.*, 2025.
- [39] J. Hu *et al.*, “Squeeze-and-excitation networks,” in *CVPR*, 2018.
- [40] B. Jacob, S. Kligys, B. Chen, M. Zhu, M. Tang, A. Howard, H. Adam, and D. Kalenichenko, “Quantization and training of neural networks for efficient integer-arithmetic-only inference,” in *CVPR Workshops*, 2018.
- [41] P. Tschandl *et al.*, “The ham10000 dataset,” *Sci. Data*, 2018.
- [42] C. Li *et al.*, “Improved efficientnet-b4 for melanoma detection,” in *ICBAIE*, 2021.
- [43] P. N. Srinivasu *et al.*, “Classification of skin disease using mobilenetv2 and lstm,” *Sensors*, 2021.
- [44] G. K. Murugesan *et al.*, “Multidimensional and multiresolution ensemble networks for brain tumor segmentation,” in *MICCAI BrainLesion Workshop*, 2019.
- [45] M. Amin-Naji *et al.*, “Ensemble of cnn for multi-focus image fusion,” *Inf. Fusion*, 2019.



Haitian Wang received the B.Eng. degree in Internet of Things Engineering from Northwestern Polytechnical University, Xi'an, China, in 2019, the M.Eng. degree in Computer Technology from Northwestern Polytechnical University in 2022, and the M.P.E. (Software) degree from The University of Western Australia (UWA) in 2024. He is currently a Research Scientist with the Department of Primary Industries and Regional Development (DPIRD), Western Australia, and a Research Associate with UWA. He will commence the Ph.D.

degree in Computer Science at UWA in 2026 and his research interests include LiDAR point cloud processing, spatial modeling, geo-registration of unstructured data, and multispectral remote sensing for precision agriculture.



Xinyu Wang received the B.I.T. degree in Networking and Cybersecurity from the University of South Australia in 2018, and the B.Sc. (Hons.) and M.I.T. degrees from The University of Western Australia (UWA) in 2024. He will commence the Ph.D. degree in Computer Science at UWA in 2025 and is currently a Research Officer and casual teaching staff member at UWA. His research interests include 3D point cloud processing, LiDAR-based spatial modeling, geo-referencing of unstructured data, urban scene reconstruction, and geospatial machine

learning.



Yiren Wang received the B.Sc. degree in Mathematics from Trinity Western University, Canada, in 2020, and the M.D.S. degree from The University of Western Australia (UWA) in 2024, where he also served as a teaching assistant. His research interests include deep learning, computer vision, natural language processing, and differential geometry. He has undertaken multiple industry experience in AI communications, education technology, and software engineering, leading to several published and deployed projects in multimodal sensing, LLM evaluation, and intelligent agent systems.



Zichen Geng received the B.E. degree from Shanghai Jiaotong University, China, and the M.S. degree from the University of Western Australia, Australia, where he is currently pursuing the Ph.D. degree in Computer Science under the supervision of Prof. Ajmal Mian and A/Prof. Wei Liu. His research interests include 3D computer vision, human motion analysis, AI for protein modeling, and generative models. He has published papers in top venues such as AAAI and ICRA, and has served as a reviewer for leading conferences including CVPR, ICCV, ICLR.



Xian Zhang received the B.Eng. and M.Eng. degrees from the Chengdu University of Information Technology (CUIT), Chengdu, China, and is currently pursuing the Ph.D. degree at The University of Western Australia (UWA), Perth, Australia. His master's research focused on generative adversarial networks (GANs), image generation, and image inpainting. His doctoral research centers on video understanding and multimodal learning. He has published several papers in leading journals, including Pattern Recognition, IEEE Transactions on Multimedia (TMM), and Applied Soft Computing.



Yu Zhang (Senior Member, IEEE) received the Ph.D. degree in Computer Science from Northwestern Polytechnical University, Xi'an, China, and RMIT University, Melbourne, VIC, Australia. He was a scholarship researcher with The University of Melbourne. He is currently a Professor with the School of Computer Science, Northwestern Polytechnical University. His research interests include ubiquitous operating systems, real-time scheduling, and edge/embedded AI. He is a Senior Member of the IEEE and a member of the ACM.



Bo Miao received his PhD degree from The University of Western Australia in 2025. He is currently a Postdoctoral Researcher at the Australian Institute for Machine Learning (AIML), The University of Adelaide. His research interests include multimodal learning, computer vision, machine learning, and video understanding. He has published papers in leading venues such as NeurIPS, ICCV, ECCV, IJCAI, IEEE Transactions on Image Processing, IEEE Transactions on Multimedia, and IEEE Transactions on Circuits and Systems for Video Technology.